energies

MDPI

Article

A High-Frequency Isolation (HFI) Charging DC Port Combining a Front-End Three-Level Converter with a Back-End LLC Resonant Converter

Guowei Cai *, Duolun Liu, Chuang Liu, Wei Li and Jiajun Sun

School of Electrical Engineering, Northeast Electric Power University, Jilin 132012, China; liuduolun@yahoo.com (D.L.); victorliuchuang@163.com (C.L.); 18686775888@163.com (W.L.); 17758885885@163.com (J.S.)

* Correspondence: caigw@neepu.edu.cn; Tel.: +86-138-4322-5886

Received: 21 July 2017; Accepted: 11 September 2017; Published: 22 September 2017

Abstract: The high-frequency isolation (HFI) charging DC port can serve as the interface between unipolar/bipolar DC buses and electric vehicles (EVs) through the two-power-stage system structure that combines the front-end three-level converter with the back-end logical link control (LLC) resonant converter. The DC output voltage can be maintained within the desired voltage range by the front-end converter. The electrical isolation can be realized by the back-end LLC converter, which has the bus converter function. According to the three-level topology, the low-voltage rating power devices can be adapted for half-voltage stress of the total DC grid, and the PWM phase-shift control can double the equivalent switching frequency to greatly reduce the filter volume. LLC resonant converters have advance characteristics of inverter-side zero-voltage-switching (ZVS) and rectifier-side zero-current switching (ZCS). In particular, it can achieve better performance under quasi-resonant frequency mode. Additionally, the magnetizing current can be modified following different DC output voltages, which have the self-adaptation ZVS condition for decreasing the circulating current. Here, the principles of the proposed topology are analyzed in detail, and the design conditions of the three-level output filter and high-frequency isolation transformer are explored. Finally, a 20 kW prototype with the 760 V input and 200–500 V output are designed and tested. The experimental results are demonstrated to verify the validity and performance of this charging DC port system structure.

Keywords: electric vehicle station; charging DC port; high-frequency isolation (HFI); three-level buck converter; LLC resonant converter

1. Introduction

As solutions of energy crisis and environmental pollution, EVs that can run on alternative resources of energy have increasingly attracted attention for investigations of decreasing fossil fuel consumption and reducing greenhouse gas emissions [1,2]. The commercial success of EVs relies heavily on the presence of high-efficiency charging stations to increase mileage and shorten charging time [3–5]. Electric vehicle technologies involved with hybrid electric vehicles (HEVs), plug-in hybrid electric vehicles (PHEVs), and plug-in pure electric vehicles (PPEVs), such as the Toyota Prius and Lexus RX 400h, have been commercialized and are available in the market. A large number of high-power charging stations need to be constructed to solve consumers' need for long-distance transport with electric vehicles (EVs). The construction of these facilities is a key factor in attracting more consumers to the use of EVs [6–10].

Recently, a distributed generation system, including the solar photovoltaic and wind power generation system as green energy, is playing an increasingly important role in energy structures. The combination of renewable energy sources with EV charging stations and energy storage systems is

inevitable [11–15]. A high-efficiency, high-power-density, high-reliability, and cost-effective charging station, depicted in Figure 1, has been designed [16–18]. Additionally, a power electronics transformer (PET) can serve as the interface between medium- and low-voltage levels [19].

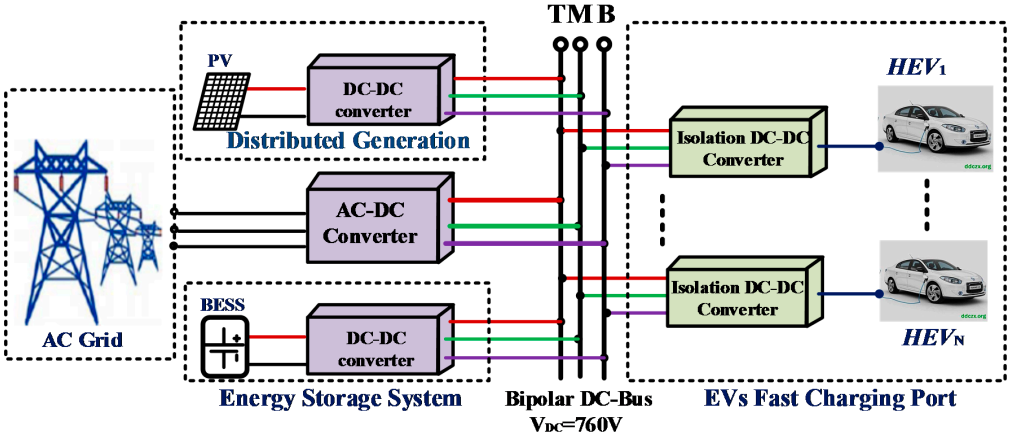

Figure 1. System block diagram of a fast electric vehicle (EV) charging station based on the common DC bus.

Chargers can be classified by two types—the on-board charger, located on the vehicle itself, and the off-board charger, which is distinct from the actual vehicle—each of which can be classified into three power levels reflecting charging characteristics shown in Table 1 by the Society of Automotive Engineers (SAE) [20–23]. It can be found that the on-board charger can draw AC current from any available power outlet and can efficiently charge the batteries. However, drawbacks, including a long charging time, low efficiency, and low reliability, are apparent. In addition, the on-board charger located on the vehicles can add volume and weight. Since a normal 3.3 kW charging power requires a 6–8 h charging time, most users have no choice but to recharge overnight. The off-board charger, called a fast-charger, can directly draw power from the DC bus, which can provide sufficient power for vehicles within a short period of time. For a normal 50 kW charging power, the Nissan Leaf, with its 24 kWh battery pack, takes only half an hour to recharge. The off-board charger has certain advantages compared with the on-board charger, such as a high power density and a high efficiency. The high-frequency-isolated DC-DC converters with a high power capacity are preferable to EVs' off-board chargers in terms of satisfying the safety requirements of charging multiple EVs within an acceptable period of time [24–30].

Table 1. Converter specifications and requirements.

Charger Location		Level 1	Level 2	Level 3
On-board chargers	V_{ac}	120 V	240 V	-
	I_{ac}	12 A	80 A	-
	P_{level}	1.4 kW	<19.2 kW	>20 kW
Off-board chargers	V_{dc} (V)	$V_{dc} \leq 450$	$V_{dc} \leq 450$	$V_{dc} \leq 600$
	I_{dc} (A)	$I_{dc} \leq 80$	$I_{dc} \leq 200$	$I_{dc} \leq 400$
	P_{level} (kW)	$P_{level} \leq 36$	$P_{level} \leq 90$	$P_{level} \leq 240$

In recent years, phase-shift full-bridge (PSFB) has become a popular topology for charging, but there are some obvious defects for a traditional zero-voltage-switching (ZVS) PSFB DC-DC converter. One is that ZVS cannot be achieved under light load conditions due to the limited ZVS range for lagging-leg switches. Another defect is the excessive conduction loss caused by the primary reflected current from the output inductor current [30]. The dual active bridge (DAB) converter is also a useful topology for high-power applications. It is difficult to achieve the ZVS of all active switches in

the DAB converter, as the switch stress is raised in this condition. Although some switching control strategies can improve this problem, this complex modulation increases the burden for the controller and for researchers [31–33].

This paper proposes a high-frequency isolation (HFI) charging DC port topology. It can serve as the interface between unipolar/bipolar DC buses and electric vehicles (EVs) through the two-power-stage system structure, which combines a front-end three-level buck converter with a back-end LLC resonant converter. The DC output voltage can be regulated within the desired voltage range by the front-end three-level buck converter. Zero-voltage switching (ZVS) for the inverter side and zero-current switching (ZCS) for the rectifier side can be realized by the back-end LLC resonant converter. In Section 2, principles of the proposed charging port topology are explored in detail. In Section 3, the features and characteristics are analyzed. In Section 4, the design conditions of the three-level output filter and high-frequency isolation transformer are explored. In Section 5, a 20 kW prototype is designed and tested. The experimental results are presented to verify the validity and performance of the proposed fast-charging DC port system structure.

2. High-Frequency-Isolation Charging Port Topology

The structure of the proposed two-power-stage system for the EV's HFI charging port is shown in Figure 2. It combines the front-end three-level buck converter, which has the ability of regulating the output DC voltage, with the back-end LLC resonant converter, which experiences high-frequency electrical isolation. Additionally, the input terminals (T, M, B) of the three-level converter can flexibly fit the bipolar DC bus or unipolar DC bus.

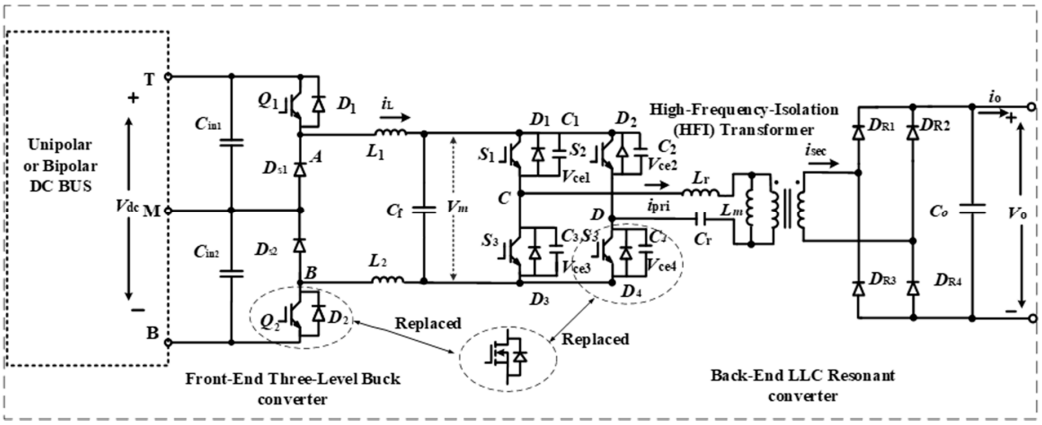

Figure 2. The proposed high-frequency isolation (HFI) charging-port topology based on a front-end three-level converter and a back-end LLC resonant converter.

The main features of the system are illustrated as follows:

(1) According to the three-level converter, the low-voltage level rating power switches can be adapted/selected for the half-voltage stress of total DC bus. Additionally, the proposed system structure can be practical under high-voltage and high-power conditions.

(2) The PWM phase-shift control for the front-end three-level buck converter can double the equivalent switching to greatly reduce the intermediate output LC filter volume.

(3) The proposed structure can regulate the DC power balance without extra balancing circuits when the input terminals (T, M, B) are interfaced with the bipolar DC bus.

(4) The back-end LLC resonant converters have the advance characteristics of zero-voltage switching (ZVS) of the inverter side and zero-current switching (ZCS) of the rectifier side. In particular, it can achieve better performance under quasi-resonant frequency mode, which greatly decreases the loss of switches.

(5) The magnetizing current of LLC high-frequency transformer can be automatically modified by following the different DC output voltages, which have the self-adaption ZVS condition for decreasing the circulating current.

2.1. Front-End Three-Level Buck Converter

Figure 3 shows the circuit diagram of the front-end three-level buck converter, which consists of two power switches (Q_1, Q_2) with the freewheeling diodes (D_{s1}, D_{s2}), the split DC-link capacitors (C_{in1}, C_{in2}), and the intermediate *LC* filter (L_{f1}, L_{f2}, C_f).

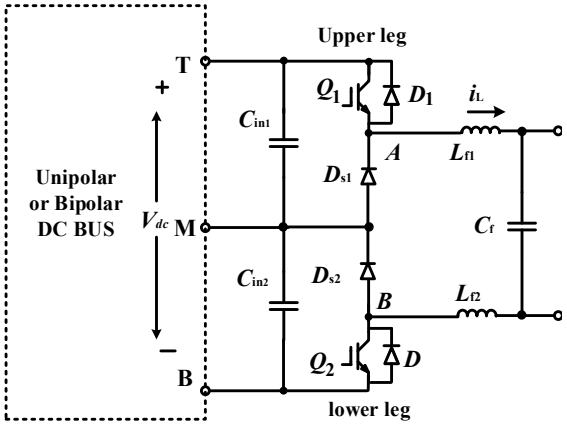

Figure 3. Front-end three-level buck converter topology.

2.1.1. Operating Principle

As shown in Figure 3, two switches (Q_1, Q_2) of the three-level buck converter are modulated by the PWM phase-shift control with the same duty cycle *D*. Figure 4a shows the converter operating waveforms for $D < 0.5$. Figure 4b shows the operating waveforms for $D = 0.5$, and Figure 4c shows the operating waveforms for $D > 0.5$. It can be found in Figure 4 that the equivalent frequency of filter inductor current i_L is twice the device switching frequency. When $D = 0.5$, this feature can reduce the output filter volume when the current ripple Δi_L for the filter inductor is nearly zero.

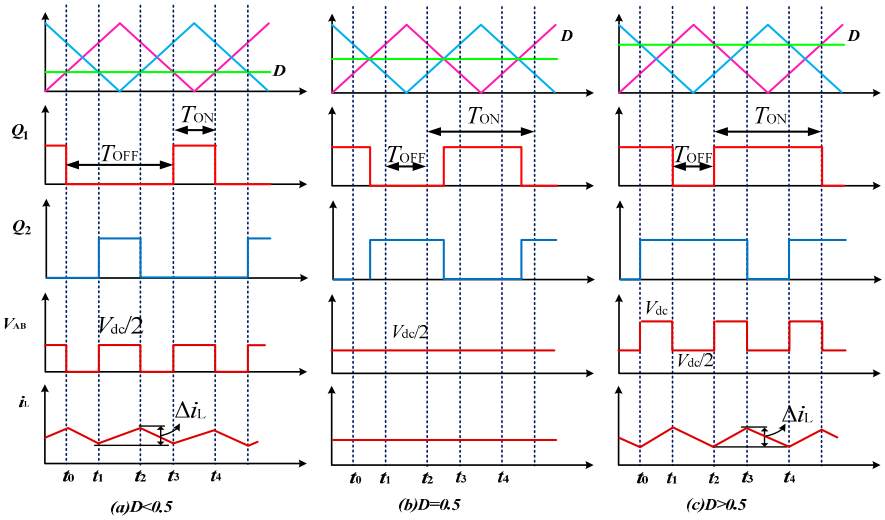

Figure 4. Main theoretical waveforms of the front-end three-level buck converter. (**a**) $D < 0.5$; (**b**) $D = 0.5$; (**c**) $D > 0.5$.

Figure 5 shows the four operating stages' ((A) t_0–t_1, (B) t_1–t_2, (C) t_2–t_3, (D) t_3–t_4) equivalent circuits for $D > 0.5$. It can be found that there are three switching modes:

Mode 1: When Q_1 is turned on and Q_2 is turned off, the generated voltage V_{AB} is half of the DC side voltage 0.5 V_{dc};

Mode 2: When Q_1 and Q_2 are turned on at the same time, the generated voltage V_{AB} is the total DC side voltage V_{dc};

Mode 3: When Q_1 is tuned off and Q_2 is turned on, the generated voltage V_{AB} is half the DC side voltage 0.5 V_{dc}.

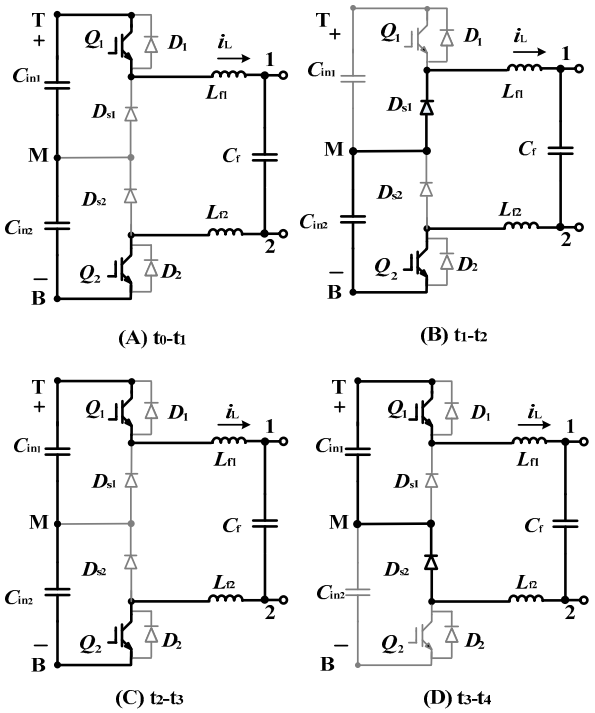

Figure 5. Operating stages and equivalent circuits for $D > 0.5$.

Figure 6 shows the equivalent circuits of two stages ((A) t_0–t_1, (B) t_1–t_2) in the half cycle for $D = 0.5$. Q_1 and Q_2 are conducting alternatively. Hence, the generated voltage V_{AB} is half of the DC side voltage 0.5 V_{dc}.

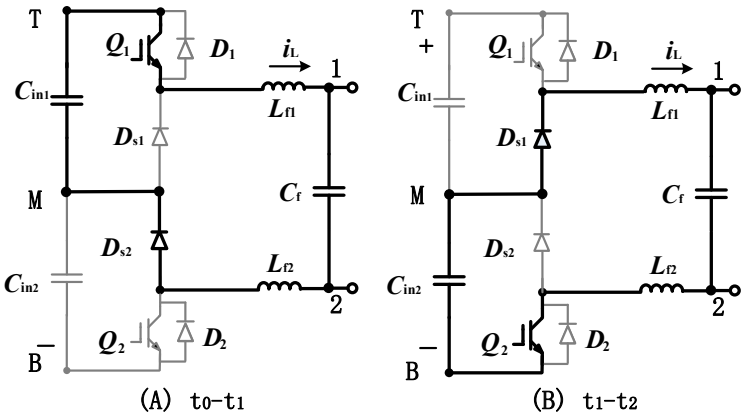

Figure 6. Operating stages and equivalent circuits for $D = 0.5$.

Figure 7 shows the four operating stages ((A) t_0–t_1, (B) t_1–t_2, (C) t_2–t_3, (D) t_3–t_4) equivalent circuits for $D < 0.5$. The three models are as follows:

Mode 1: When Q_1 is turned off and Q_2 is turned off at the same time, the generated voltage V_{AB} is 0;
Mode 2: When Q_1 is turned off and Q_2 is turned on, the generated voltage V_{AB} is half of the DC side voltage 0.5 V_{dc};
Mode 3: When switch Q_1 is turned on and Q_2 is turned off, the generated voltage V_{AB} is half of the DC side voltage 0.5 V_{dc}.

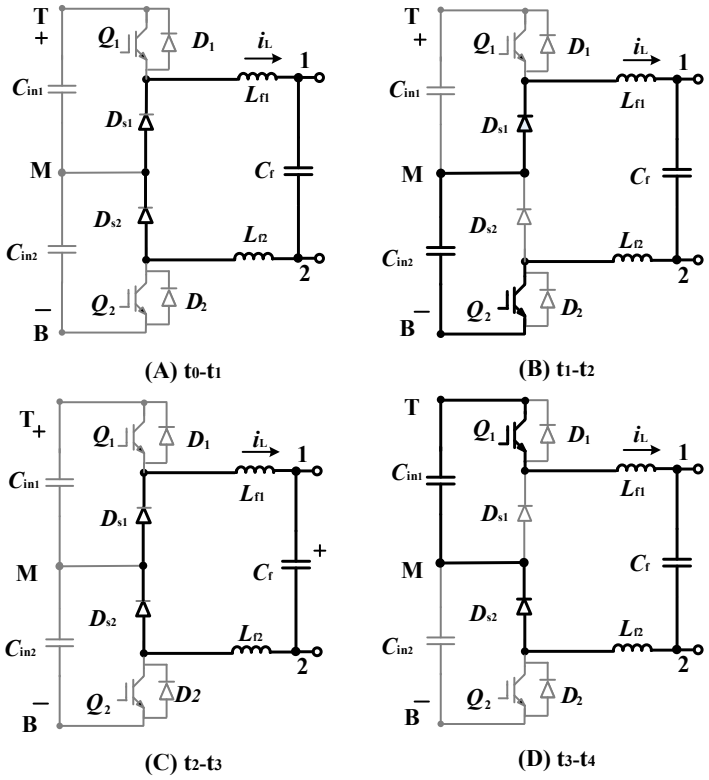

Figure 7. Operating stages and equivalent circuits for $D < 0.5$.

2.1.2. The Inductor Current Ripple Analysis

The converter output inductor current ripple Δi_L is derived for $D > 0.5$ and $D < 0.5$, respectively, through the operating waveforms, as shown in Figure 4 [34,35].

$$\Delta i_L = \begin{cases} \frac{(1-D)(2D-1)V_{dc}T}{2(L_1-L_2)} & D \geq 0.5 \\ \frac{(1-2D)V_{dc}}{2(L_1+L_2)}DT & D < 0.5 \end{cases} \quad (1)$$

where T is the switching period, and D is the duty cycle.

Thus, the maximum output inductor current ripple Δi_{Lmax} can be expressed as follows:

$$\Delta i_{Lmax} = \frac{V_{dc}T}{16(L_1+L_2)} \quad (2)$$

Figure 8 shows the graph for the relation between the duty cycle D and the output inductor current ripple Δi_L. As can be seen, the output inductor current ripple can reach the peak value Δi_{Lmax} for $D = 0.75$ and $D = 0.25$, while the output inductor current ripple Δi_L is nearly zero for $D = 0.5$.

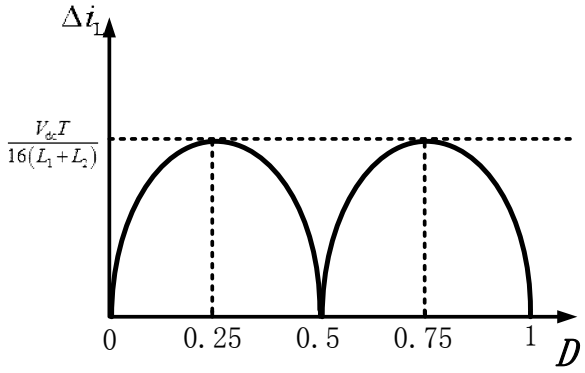

Figure 8. The relation between the duty cycle D and the output inductor current ripple Δi_L.

2.2. Back-End HFI LLC Resonant Converter

The structure of the back-end LLC resonant converter is demonstrated in Figure 9. The structure consists of the full-bridge inverter, a resonant tank, and a rectifier, which can achieve the high-frequency isolation (HFI) between the common DC bus and the EVs. The full-bridge inverter contains two parallel legs with four power switches S_1–S_4 including their anti-parallel diodes D_1–D_4 and parallel capacitors C_1–C_4. Meanwhile, the resonant tank is composed of the resonant capacitor C_r, the series resonant inductor L_r, and the high-frequency isolation (HFI) transformer, while the rectifier is composed of four diodes D_{R1}–D_{R4}. The resonant inductor L_r can be replaced by the leakage inductor of the transformer. The resonant capacitor C_r can also filter the DC component and prevent DC magnetic bias. The LLC resonant converters have advance characteristics of zero-voltage switching (ZVS) of inverter side and zero-current switching (ZCS) of the rectifier side. In particular, it can achieve better performance under quasi-resonant frequency mode and greatly reduce switching losses and improving system efficiency. The features of the back-end LLC resonant converter stated above have great advantages for power electronics transformer (PET) applications under high-voltage and high-power conditions.

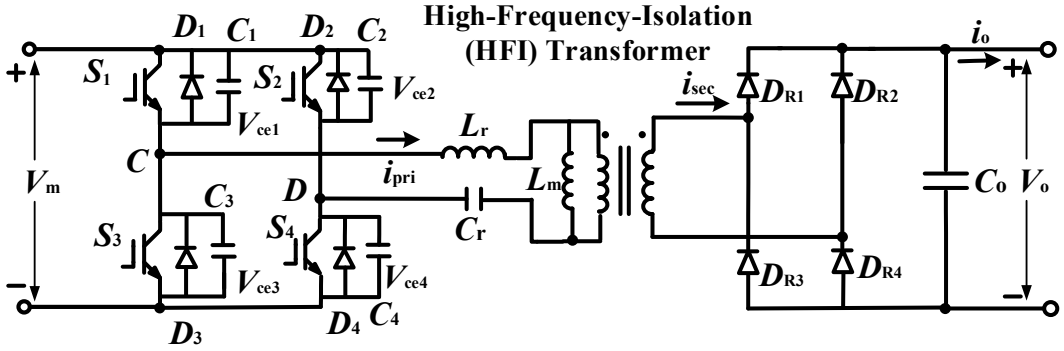

Figure 9. Back-end HFI LLC resonant converter.

2.2.1. Operating Principle

The operating principle and the key waveforms of the proposed back-end LLC resonant is shown in Figure 10, including the gate signals of active switches (S_1–S_4), the series resonant inductor current i_{pri}, the magnetizing inductor current i_m, and the output current i_{sec} on the secondary side.

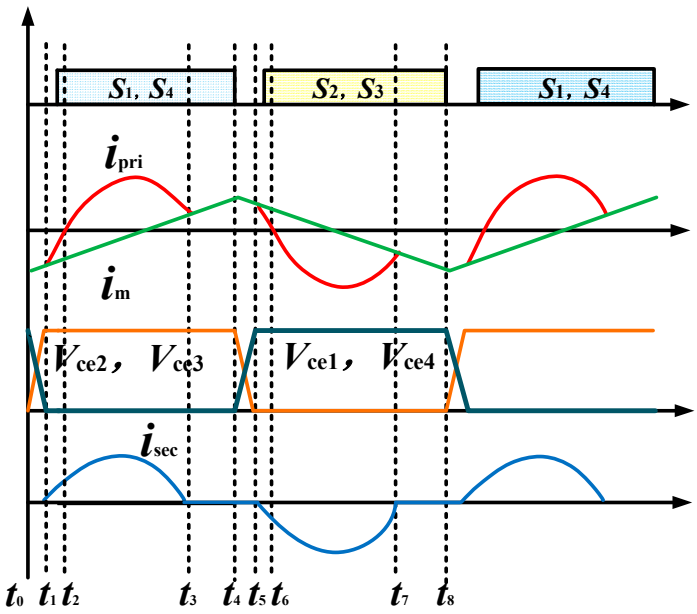

Figure 10. Operating waveforms of the back-end HFI LLC resonant converter.

As for the resonant circuit, there are eight operation modes dependent on the direction of the primary current i_{pri} and the inverter working conditions.

(1) Mode 1 (t_0–t_1)

This mode begins when S_2 and S_3 are turned off at t_0, when the resonant inductor L_r current i_{pri} flows in the negative direction. Meanwhile, the C_1 and C_4 discharge until V_{ce1} and V_{ce4} reach zero and the primary current i_{pri} decreases. In this period, the magnetizing inductor current i_m is equivalent to i_{pri}; thus, there is no induced current on the secondary side. The stored energy acquired by the output capacity C_O is transferred to the load.

(2) Mode 2 (t_1–t_2)

In this mode, the i_{pri} is still negative and will flow via the anti-parallel diodes of D_1 and D_4. The ZVS condition is achieved for S_1 and S_4. The magnetizing inductor current i_m increases linearly when i_{sec} begins to increase.

(3) Mode 3 (t_2–t_3)

This mode begins when the resonant inductor current i_{pri} becomes positive. Now, the magnetizing inductor current i_m linearly increases with the resonant L_r while the resonant capacitor C_r works in a series-resonant condition. This mode ends when i_m and i_{pri} are equal at t_3. At the same time, the output current i_{sec} decays to zero. Both rectifier diodes D_{R1} and D_{R4} are turned off and ZCS is achieved.

(4) Mode 4 (t_3–t_4)

This mode begins when the resonant inductor current i_{pri} is equal to the magnetizing inductor current i_m at t_3, and both of them increase linearly while the i_{sec} is equal to zero. In this mode, the output is separated from the high-frequency transformer and the stored energy acquired by the output capacity C_O is transferred to the load. This mode ends when S_1 and S_4 are turned off at t_4.

For the next half cycle, the operation is opposite to the analysis above.

2.2.2. Voltage Gain Characteristics of the LLC Resonant Converter

As can be seen from Figure 11, the equivalent circuit diagram works under quasi-resonant frequency, in which R_{eq} is equivalent to the AC load of DC load R. The output DC load R is replaced by the equivalent AC load R_{eq} expressed as follows [36]:

$$R_{eq} = \frac{8n^2R}{\pi^2} \tag{3}$$

where n is the transformer turn ratio.

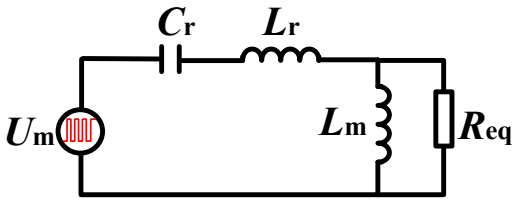

Figure 11. Equivalent circuit for the back-end LLC resonant converter.

To simplify the analysis, the input voltage can be equivalent to a square-wave voltage source U_{square}, which needs to be Fourier-transformed:

$$U_{square}(\omega t) = \sum_{k=1}^{\infty} u_{sin}(k\omega t) = \frac{4U_m}{\pi}(\sin\omega t + \frac{1}{3}\sin 3\omega t + \cdots) \tag{4}$$

Sinusoidal steady-state analysis is required for the equivalent electrical circuit. The output voltage $\dot{U}_{kout}$ under the $k\omega$ frequency condition can be obtained by

$$\dot{U}_{kout} = \frac{\dot{U}_m(x_{Lm}//R_{eq})}{X_{Cr} + X_{Lr} + (X_{Lm}//R_{eq})} = \frac{U_{sin}k\omega\frac{jk\omega L_m R_{eq}}{jk\omega L_m + R_{eq}}}{\frac{1}{jk\omega C_r} + jk\omega L_r + \frac{jk\omega L_m R_{eq}}{jk\omega L_m + R_{eq}}} \tag{5}$$

Then, the instantaneous value of the output voltage $u_{out}(t)$ is given by

$$u_{out}(t) = \sum_{k=1}^{\infty} u_{kout}(k\omega t) \tag{6}$$

The RMS of output voltage U_{out} yields

$$U_{out} = \sqrt{U_{1out}^2 + U_{2out}^2 + U_{3out}^2 + \cdots} \tag{7}$$

Hence, the LLC resonant converter voltage gain G is

$$G = \frac{U_{out}}{U_m} \tag{8}$$

where U_m is the RMS of the square-wave voltage source.

The value of L_r is the intrinsic parameter of the transformer, and the values of L_m and C_r are calculated by Equation (11). An LLC resonant converter with a 44 kHz resonant frequency has been designed, and the key parameters are L_r = 9.7 μH, L_m = 230 μH, and C_r = 1.32 μH. The experimental voltage gain characteristics of the LLC resonant converter under different load scenarios are shown in Figure 12 through the frequency response analyzer (VENABLE Model 3120). As can be observed in Figure 12, the LLC resonant converter shows the voltage gain characteristics, which are almost independent of the load when the switching frequency f_s is around the resonant frequency f_r called

a quasi-resonant frequency. This is a distinct advantage of LLC resonant converter compared to the other DC-DC converters.

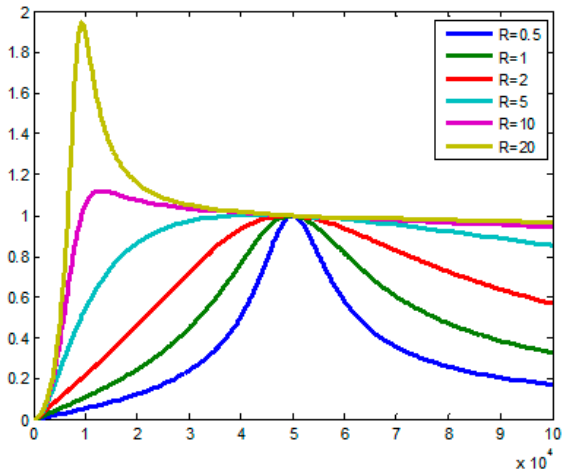

Figure 12. Voltage gain characteristics of LLC resonant converters.

3. Features and Characteristics

3.1. Three-Level Buck Converter Working at Higher DC Modulation Index

The three-level buck converter is placed in front of the LLC resonant converter, which can help to obtain the desired output voltage with the higher modulation index D_1 expressed in Equation (9) comparison to the other DC-DC converters:

$$D_1 = \frac{V_o}{V_{dc}} n \tag{9}$$

The DC modulation index D_2 of the traditional DC converter given by

$$D_2 = \frac{V_o}{V_{dc}} \tag{10}$$

where V_o is the output voltage, V_{dc} is the input voltage, and n is the transformer turn ratio. A step-down transformer ($n > 1$) has been used; hence, $D_1 > D_2$.

Taking the input voltage V_{dc} = 760 V and the output voltage V_o range from 200 to 500 V of the HFI DC–DC converter as an example. If $n = 760/500$, after the aforementioned calculation, the range of DC modulation index D_1 is from 0.4 to 1, while the range of the DC modulation index D_2 is from 0.26 to 0.65. Thus, the front-end three-level buck converter working at higher DC modulation index increases the voltage utilization ratio and improves efficiency.

3.2. The Proposed DC Charging Port Having Different Power Balancing Capability for a Bipolar DC Bus

The split DC-link capacitors (C_{in1}, C_{in2}) connected on three-level buck converter are used as the interface between the bipolar DC buses. If there is a power imbalance in the bipolar DC bus, changing the DC modulation index of the upper and lower legs can balance the power between the DC buses. Figure 13 shows a diagram of power balance management. If the power on the positive DC side is higher than the negative DC side, it is necessary to increase the DC modulation index of the upper leg and reduce the DC modulation index of the lower leg. Therefore, the fast charger discharges more power from the positive to balance the bipolar DC bus. Alternatively, if the power on the positive DC side is less than the power on the negative DC side, it can balance the bipolar DC bus by adjusting the modulation index of the upper and lower legs.

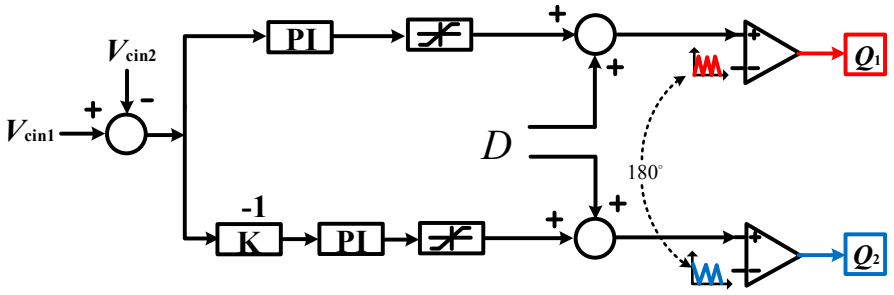

Figure 13. Modulation block diagram of the front-end three-level buck converter.

3.3. LLC Resonant Converter Having ZVS Conditions with Different Magnetizing Current at Different Output Voltages

There is a condition for achieving ZVS:

The energy stored in the magnetizing inductor is larger than the energy stored in the switch parallel capacitance. According to [37], a generalized expression for magnetizing inductance is derived as

$$L_m < \frac{v_{in}}{N v_{out}} \cdot \frac{t_d}{16 C_1 f} \tag{11}$$

where t_d is the dead-time interval, N is the ratio of transformer, and C_1 is the parasitic capacitance.

The structure of the proposed HFI charging port is shown in Figure 2. When the DC modulation index of front-end three-level buck converter was charged, the middle voltage V_m will also be changed, causing the magnetizing inductor current i_m to change. The simulation waveforms of magnetizing inductor i_m under different inverter output voltages (V_{CD}) are shown in Figure 14. It can be clearly seen that i_m is changing with V_{CD}, but the ZVS can be achieved by the magnetizing inductor L_m by drawing energy from the parallel capacitors C_1–C_4 until the energy stored in the parallel capacitance discharged thoroughly. This is because the voltage of parallel capacitor V_{cex} decreases to zero during the dead time, as the converter has the self-adaption ZVS condition.

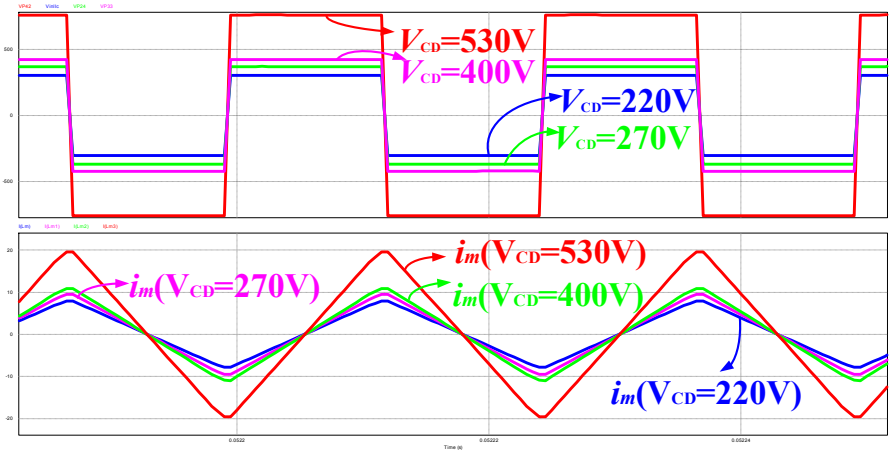

Figure 14. Simulation waveform of magnetizing inductor current under different V_{CD} values.

3.4. LLC Resonant Converter Containing Constant Current at Different Output Voltages with the Same Charging Current Command

As the proposed back-end LLC resonant converter directly transfers power to the EV's batteries, the output current remains constant whenever the output voltage changes in constant-current charging mode. The battery terminal voltage increases when the output current remains constant, while the input voltage V_m of LLC resonant converter increases along with the output voltage V_o, causing the

magnetizing inductor current i_m to also increase. In order to maintain the output current i_o constant following the output voltage increasing, the resonant current i_{pri} increases a little along with the magnetizing inductor current i_m. Therefore, the resonant current waveform is not affected by the output voltage V_o. On the contrary, if the LLC resonant converter is placed at the front end and is connected directly to the DC bus, the LLC input voltage V_{in} is clamped at the DC bus voltage V_{dc}. Thus, it keeps constant and the waveform of magnetizing inductor current is also constant. In this condition, the input current inevitably changes with the output voltage fluctuates in constant-current charging mode. Thus, the whole resonant process could not be optimized in different power conditions.

4. Design Conditions

4.1. Front-End Three-Level Buck Converter Inductor Filter Design

The maximum value of the filter inductor current ripple Δi_{Lmax} can typically be 10–30% of the peak current:

$$\Delta i_{Lmax} = \frac{V_{dc}T}{16(L_1 + L_2)} \tag{12}$$

Thus, the total filter inductor L_f can be derived as

$$L_f = L_1 + L_2 = \frac{V_{dc}T}{16\Delta I_{Lmax}} \tag{13}$$

The Δi_L reaches the maximum value for the duty cycle D = 0.25 and D = 0.75. A 20 kW prototype with a 760 V input DC voltage and a 200–500 V output DC voltage with a working frequency of f_s = 20 kHz was built and tested. Based on the calculation above ΔI_{Lmax} = 6 A, the filter inductor $L_1 = L_2$ = 200 μH can be derived. The next step is to select a suitable magnetic core and calculate the desirable turns N.

The front-end three-level buck converter can increase the equivalent switching twice using the PWM phase-shift control, so the frequency of inductor current ripple is 40 kHz. The formula of the Kool Mu window area W_a is derived as follows [38]:

$$W_a A_e \geq \frac{L I_{rms} I_{pk}}{J B_m K_u} 10^4 \tag{14}$$

where the utilization rate of the window K_u is 0.5, and the maximum magnetic flux density B_m is 0.45 T. The current density J is 400 A/cm^2. A_ε is the cross area of the wire.

Hence, according to $W_{a1}A_{e1}$ > 341 cm^4, $W_{a1}A_{e1}$ = 350 cm^4 is better for designing a necessary inductor in the Power Electronics Laboratory based on actual engineering problems. A magnetic core K8020E060 was selected, of which the window area W_{a2} is 11.1 cm^2, and the cross-sectional area A_{e2} is 3.89 cm^2. The number of magnetic core S can be shown to be

$$S = W_{a1}A_{e1}/W_{a2}A_{e2} \tag{15}$$

Based on Equation (15), the number S is 8. The inductor L can be denoted as

$$L = SA_L N^2 \tag{16}$$

where A_L is 190 nH; thus, the number of turns N = 17.

The experimental filter inductor prototype in accordance with the theoretical analysis mentioned above is presented in Figure 15.

Figure 15. Front-end three-level buck converter inductor filter.

4.2. Back-End LLC Converter ZVS Condition

For the back-end LLC resonant converter switches (S_1–S_4), the ZVS condition can satisfy from zero to full-load conditions because the magnetizing current i_m shown in Equation (17) is independent of the loads:

$$i_m = \frac{V_{in}}{4L_m f_s} \tag{17}$$

The input voltage V_{in} of the LLC resonant converter is clamped to the front-end buck converter regulated by the DC modulation index. The energy stored in the magnetizing inductor is sufficient for achieving ZVS for switches (S_1–S_4) within the voltage range. In this condition, another key point is regulating the dead time to satisfy the condition under which the energy stored in parallel capacitance can decay thoroughly.

4.3. High Frequency LLC Transformer Design

The high-frequency electrical isolation can be realized by the high-frequency transformer, which is the main component of the back-end LLC resonant converter with the bus converter function. The turn ratio n and the number of turns N are the key parameters for designing a high-frequency transformer. A 20 kW prototype with a 760 V input and a 200–500 V output DC voltages with a working frequency f_s = 40 kHz was designed, so the turn ratio n (760/500) was adopted. The peak value of input voltage E_1 can be calculated as follows:

$$E_1 = 4fN_1B_mA_{core} \tag{18}$$

where N_1 is number of turns on the primary side, A_{core} is the cross-sectional area of the main magnetic circuit of the magnetic core, B_m is the maximum flux density, and f is the working frequency.

Thus, the number of turns on the secondary side N_2 can be obtained:

$$n = \frac{N_1}{N_2} \tag{19}$$

The experimental high-frequency LLC transformer is presented in Figure 16.

Figure 16. High-frequency LLC transformer.

5. Experimental Results

The 20 kW prototype with an input voltage of 760 V and an 200–500 V output voltage, which integrates with the front-end three-level buck converter working at a frequency of 20 kHz and the back-end LLC resonant converter working at a frequency 40 kHz, was designed and tested. The experimental results are presented here to verify the validity and performance of the proposed fast-charging DC port system structure.

The photograph of the hardware prototype is shown in Figure 17, and the specifications of the prototype are shown in Table 2.

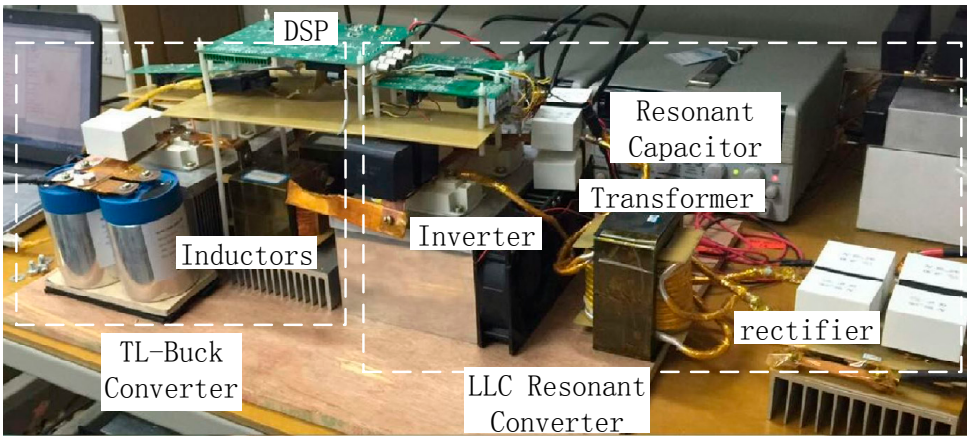

Figure 17. The HFI fast-charging DC port system experimental setup.

Table 2. Circuit parameters of the HFI fast-charging DC port system.

Description	Parameters
Input voltage V_{dc}	760 V (DC)
Output voltage V_o	200–500 V (DC)
Transformer turn ratio n	17:12
Three-level buck converter working frequency f	20 kHz
LLC resonant converter working frequency f_s	40 kHz
Resonant frequency f_r	44 kHz

In the power electronics laboratory, the ITEM number of the resonant capacitor is C4BSYBX3330Z_F_, the manufacturer is KEMET, U_n = 3000 V, and the value is 0.33 μF. The ITEM number of the rectifier diode is DSEI2X101-12A, and the manufacturer is IXYS. The ITEM number of the IGBT is SKM200GB125D,

and the manufacturer is SEMIKRON INTERNATIONAL. The ITEM number of the voltage capacitance is SHK-700-540-FS, and the manufacturer is EACO. The ITEM number of the transformer core is K8020E060.

Figure 18 shows the waveforms of the proposed HFI charging DC port with D = 0.75; the total input voltage V_{dc} = 760 V, the LLC resonant converter input voltage V_{in} = 570 V, and the output voltage V_o = 400 V; the total input current i_{dc} = 26 A, the inductor current i_L = 35 A, and the output current i_o = 50 A with the resistive DC load R_0 = 8 Ω; the output power is about 20 kW. It can be seen that the system performs well while working in the steady-state operation and the experimental results are consistent with the theoretical analysis above.

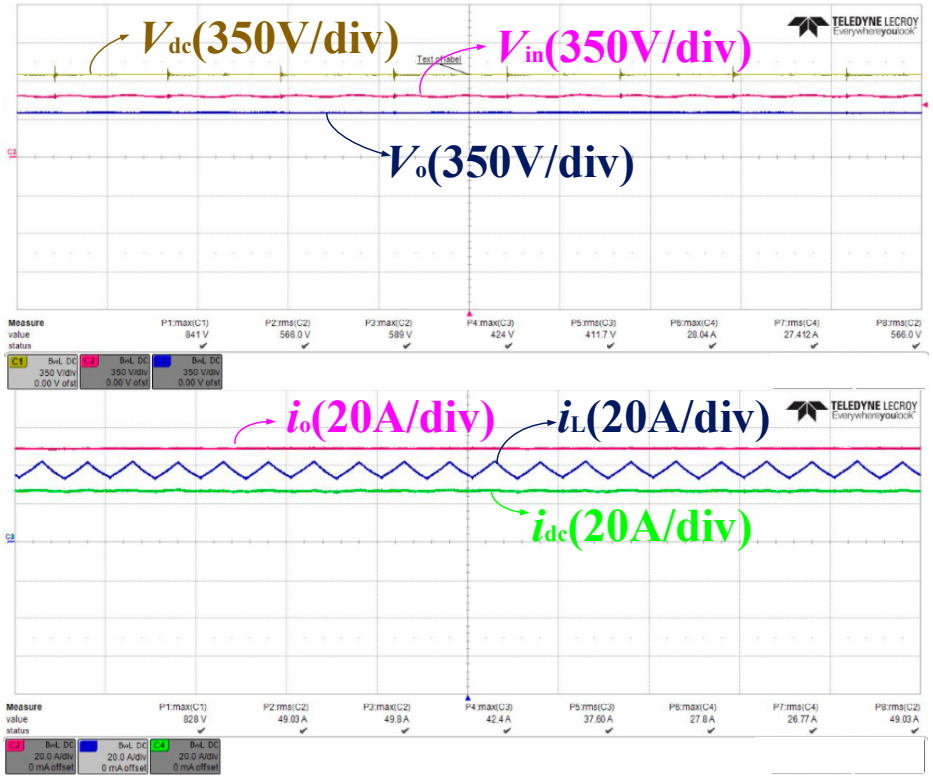

Figure 18. Experimental results of the converter in the steady-state operation.

5.1. In Steady-State Operation

Figure 19 shows the experimental waveforms of the front-end three-level buck converter output voltage V_{AB} and inductor current i_L under different DC modulation indices (D = 0.4, D = 0.5, D = 0.75). The input voltage V_{dc} = 760 V and the load R_0 = 8 Ω. As seen from Figure 20a, the V_{AB} voltage is changed between 0 (Q_1 and Q_2 are off-state, D_1 and D_2 are on-state) and 380 V (Q_1 and D_2 are on-state or Q_2 and D_1 are on-state) for D = 0.4 and the output power is about 5.7 kW. The inductor current ripple Δi_L = 3.8 A is very close to the result of Equation (1). From Figure 20b, V_{AB} is fixed at 380 V (Q_1 and D_2 are on-state or Q_2 and D_1 are on-state), and the inductor current ripple Δi_L almost reaches zero. This is because there is no voltage ripple on the filter inductors with D = 0.5, and the output power is nearly 9 kW. As can be seen from Figure 20c, V_{AB} is changed between 380 V (Q_1 and D_2 are on-state or Q_2 and D_1 are on-state) and 760 V (both Q_1 and Q_2 are on-state) for D = 0.75 with about 20 kW of the output power. It can be found that the value of the output inductor current ripple reaches the maximum value Δi_{Lmax}, which is about 6 A.

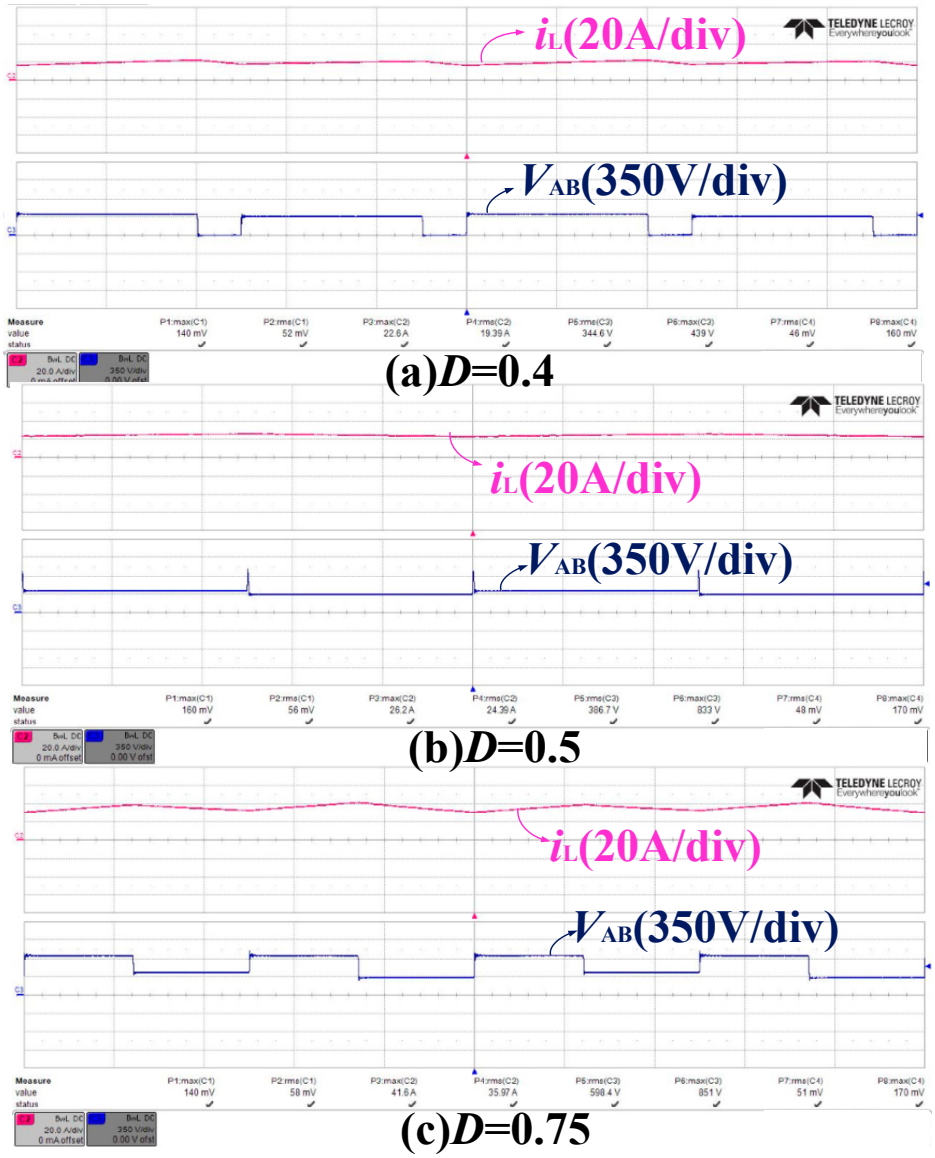

Figure 19. Experimental results of the front-end three-level buck converter (**a**) D = 0.4; (**b**) D = 0.5; (**c**) D = 0.75.

Figure 20 shows the experimental waveforms of the intermediate filter inductor current i_L, the LLC primary side current i_{pri}, the LLC secondary side current i_{sec}, and the LLC inverter-side output voltages (V_{CD}) under different front-end modulation indices (with D = 0.4 having an output power of about 5.7 kW, D = 0.5 having an output power of about 9 kW, and D = 0.75 having an output power of about 20 kW). The input voltage, V_{dc} = 760 V, and the load, R_0 = 8 Ω. It can be found that the primary side current i_{pri}, secondary side current i_{sec}, and inverter-side output voltages V_{CD} are changed due to different modulation indices. Additionally, the LLC resonant converter has good characteristics of zero-voltage switching (ZVS) with a different magnetizing inductor current i_m. The current waveforms on the primary side and secondary side present smooth curves that are consistent with the simulation results; thus, the viability and performance of the two power-stage system structure has been proved.

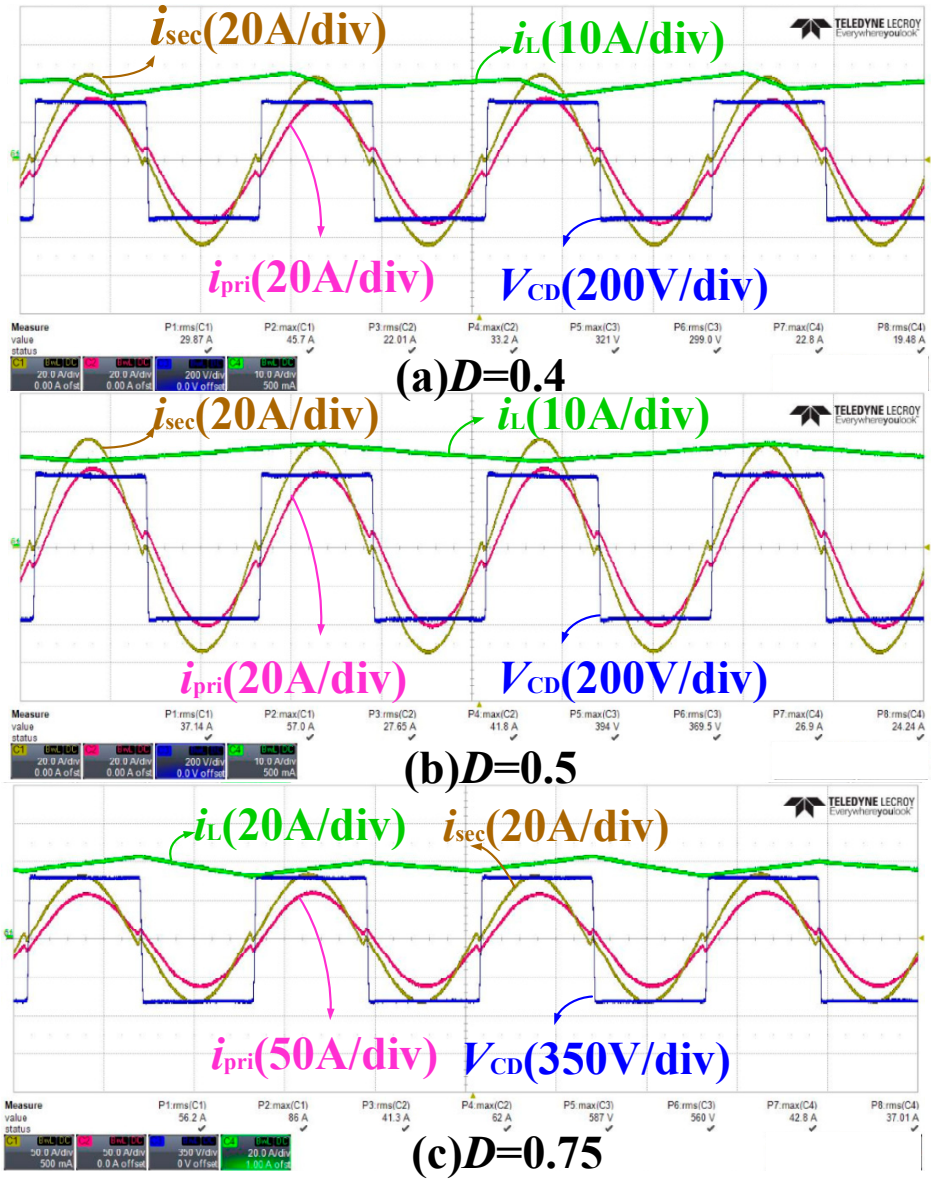

Figure 20. Experimental results of the back-end HFI LLC resonant converter (**a**) D = 0.4; (**b**) D = 0.5; (**c**) D = 0.75.

The ZVZCS characteristic curves of the back-end HFI LLC resonant converter under different modulation indices are shown in detail in Figure 21. The input voltage V_{CD} = 760 V and the load, R_0 = 8 Ω. V_{ce1} is the voltage of switch S_1 and V_{gs1} is the gate signal; i_{pri} is the primary side current and i_{sec} is the secondary side current. It can be seen from Figure 21 that V_{gs1} begins to turn on switch S_1 after the V_{ce1} decreases to zero; thus, ZVS can be achieved from zero to full-load conditions. Additionally, ZCS can be achieved when i_{sec} reaches zero at the end of the resonant process under different output voltages conditions.

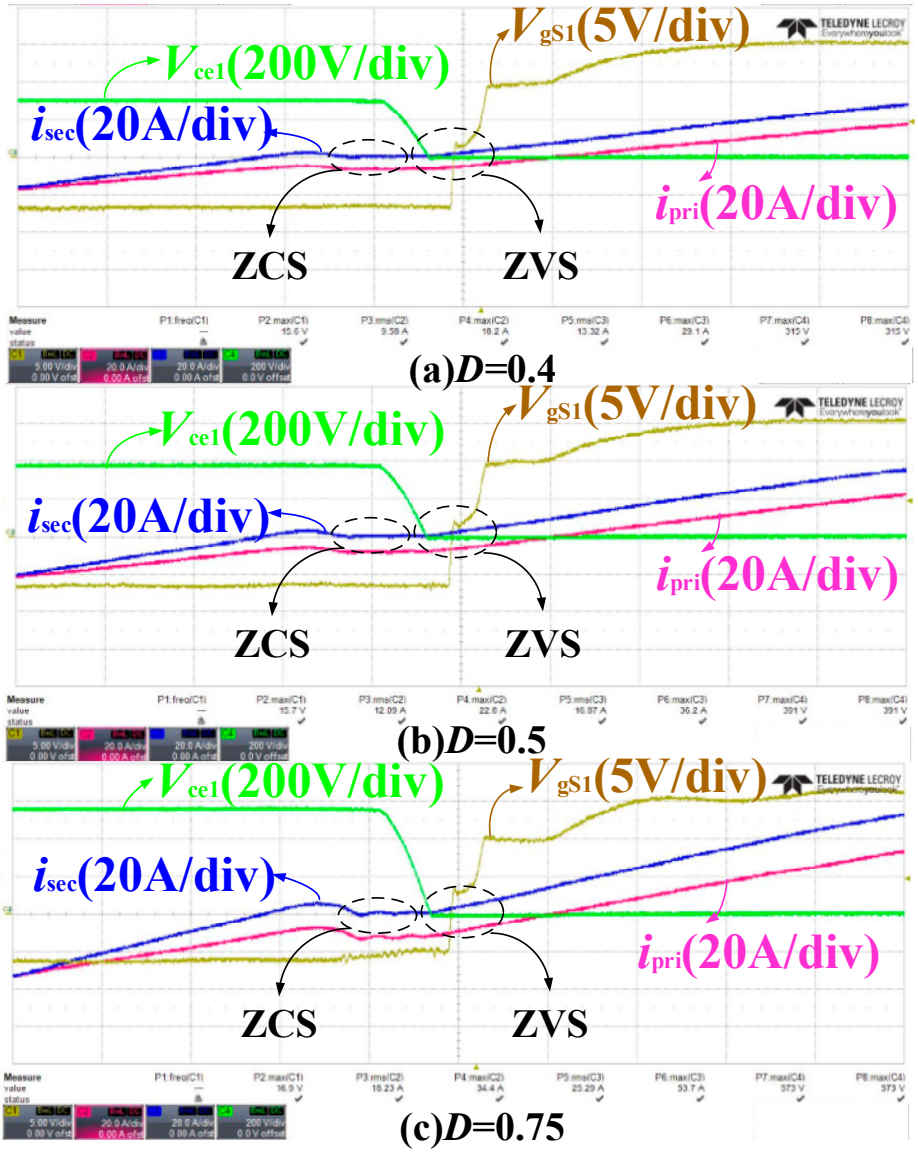

Figure 21. Back-end HFI LLC resonant converter ZVZCS characteristic curves (**a**) D = 0.4; (**b**) D = 0.5; (**c**) D = 0.75.

Figure 22 shows the experimental results of magnetizing inductor i_m current under different modulation indices D in detail under different power conditions. When the resonant process of C_r and L_r ends, the LLC primary-side i_{pri} is the same as the magnetizing inductor current i_m. It can be seen that i_m is changing with the inverter-side output voltage V_{CD}, the ZVS can be achieved adaptively and the circulating current is also decreased.

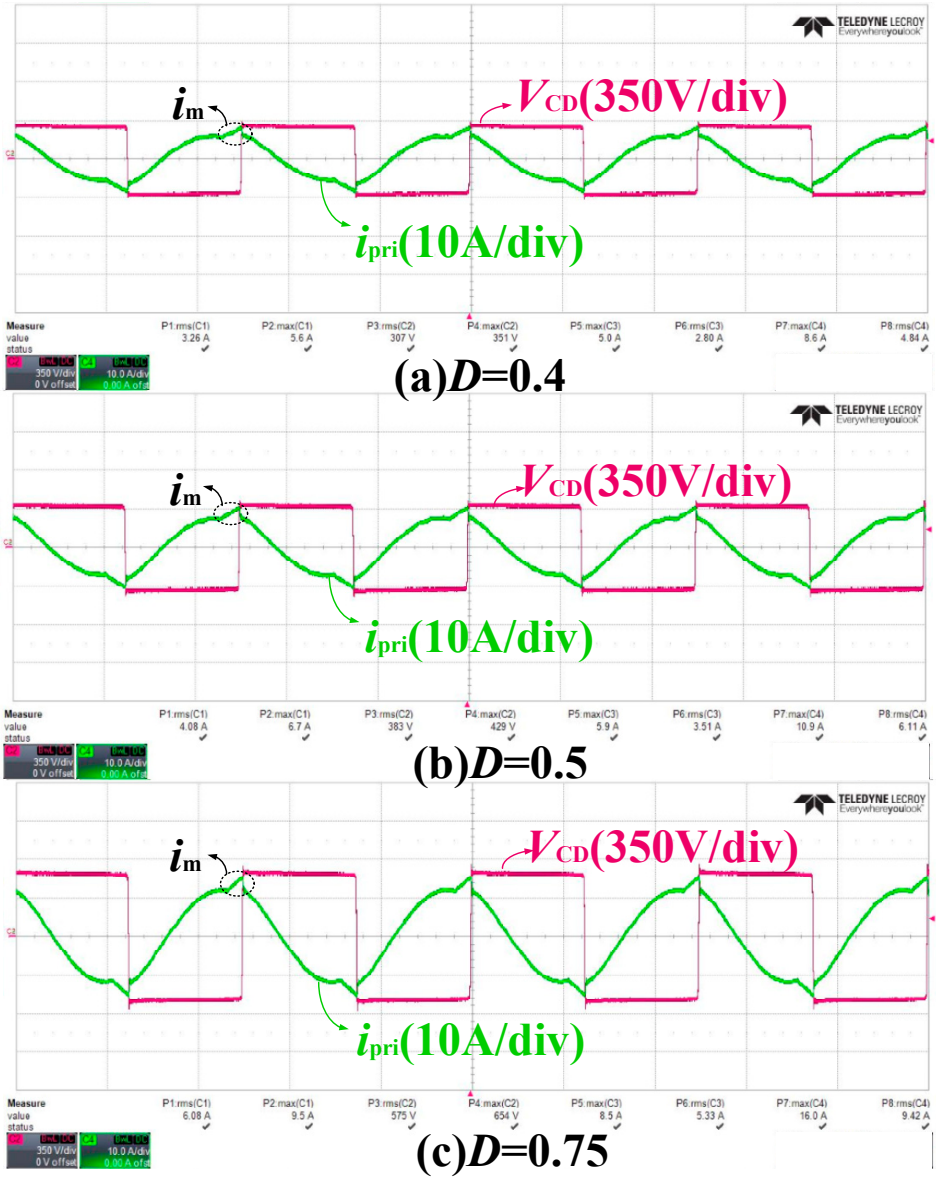

Figure 22. Experimental waveforms of the magnetizing inductor current under different modulation indices *D*.

5.2. In the Load-Step Operation

In order to verify the viability and performance of the fast-charging DC port, dynamic-state experiments have been designed with changing loads. Figures 23 and 24 show the transient experimental waveforms of the front-end three-level buck converter output voltage V_{AB}, the inductor current i_L, the LLC inverter-side output voltage V_{CD}, and the primary side current i_{pri} during a load step-up of the resistive load from 16 to 27 Ω and a load step-down of the resistive load from 27 to 16 Ω. As can be seen, the output voltages V_{AB} and inverter output voltage V_{CD} are independent of the resistive load, while the inductor current i_L and the primary side current i_{pri} reach a new stable state in a short time. Experimental results have shown that the proposed system structure can perform well under the conditions of a transient operation.

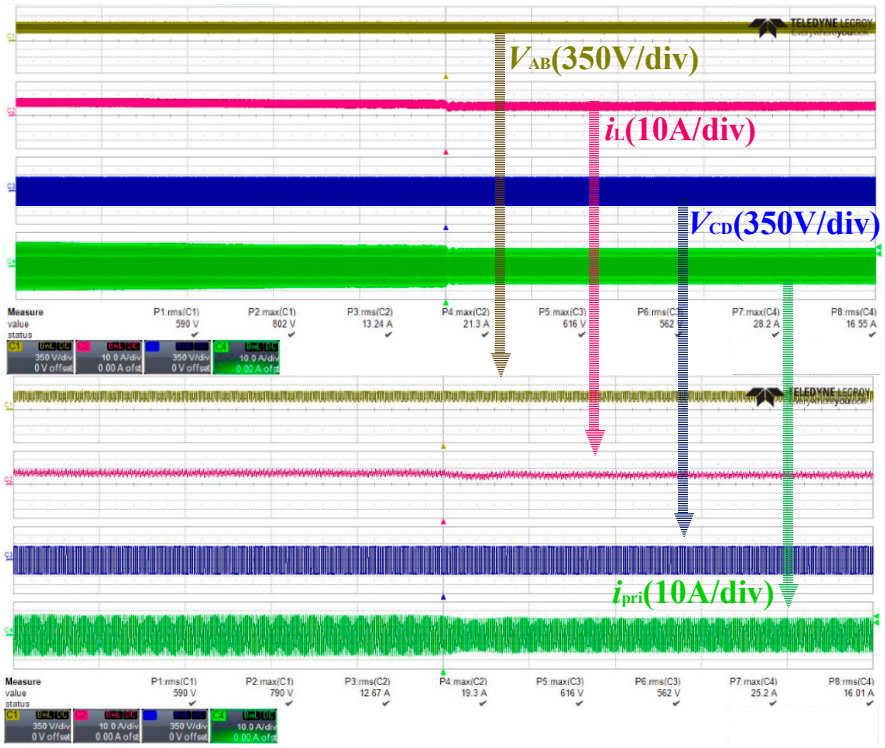

Figure 23. Transient waveforms during a step-up of resistive load from R_0 = 16 Ω to R_0 = 27 Ω.

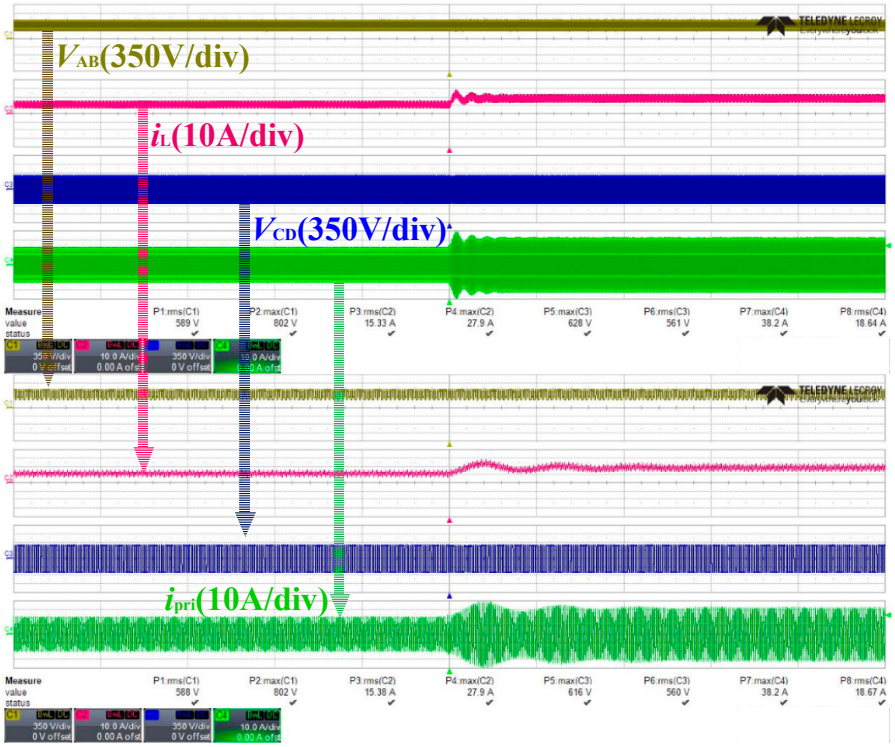

Figure 24. Transient waveforms during a step-down of the resistive load from R_0 = 27 Ω to R_0 = 16 Ω.

Finally, the experimental results above have shown the characteristic of the front-end three-level buck converter and the back-end LLC resonant converter in a steady-state operation and in a load-step

operation. The validity and performance of the proposed HFI fast-charging DC port system structure has thus been proved.

6. Conclusions

A high-frequency-isolation (HFI) charging DC port can serve as the interface between unipolar/bipolar DC buses and electric-vehicles (EVs) based on a double power-stage system structure, which combines a front-end three-level converter with a back-end LLC resonant converter. Principles of the proposed charging port topology are studied in detail, while the features and characteristics are analyzed. Then, the design conditions of the three-level output filter and high-frequency isolation transformer are explored. Finally, a 20 kW prototype is designed and tested. The experimental results are presented to verify the validity and performance of the proposed HFI fast-charging DC port system structure.

Acknowledgments: This work is supported by the Science and Technology Foundation of Department of Education of Jilin Province (No. 201414002).

Author Contributions: Guowei Cai put forward the main idea and design of the entire venation of this paper. Duolun Liu performed the experiments and prepared the manuscript. Chuang Liu, Wei Li, and Jiajun Sun guided the experiments and wrote the paper.

Conflicts of Interest: The authors declare no conflict of interest.

References

1. Tabari, M.; Yazdani, A. An energy management strategy for a DC distribution system for power system integration of Plug-In Electric Vehicles. *IEEE Trans. Smart Grid* **2016**, *7*, 659–668. [CrossRef]
2. Korolko, N.; Sahinoglu, Z.; Nikovski, D. Modeling and forecasting self-similar power load due to EV fast chargers. *IEEE Trans. Smart Grid* **2016**, *7*, 1620–1629. [CrossRef]
3. Liu, C.; Gu, B.; Lai, J.S.; Wang, M.; Ji, Y.; Cai, G.; Zhao, Z.; Chen, C.L.; Zheng, C.; Sun, P. High-efficiency hybrid full-bridge–half-bridge converter with shared ZVS lagging leg and dual outputs in series. *IEEE Trans. Power Electron.* **2013**, *28*, 849–861. [CrossRef]
4. Goli, P.; Shireen, W. PV integrated smart charging of PHEVs based on DC link voltage sensing. *IEEE Trans. Smart Grid* **2014**, *5*, 1421–1428. [CrossRef]
5. Dubey, A.; Santoso, S.; Cloud, M.P. Average-value model of electric vehicle chargers. *IEEE Trans. Smart Grid* **2013**, *4*, 1549–1557. [CrossRef]
6. Hredzak, B.; Agelidis, V.G.; Jang, M. A model predictive control system for a hybrid battery-ultracapacitor power source. *IEEE Trans. Power Electron.* **2014**, *29*, 1469–1479. [CrossRef]
7. Channegowda, J.; Pathipati, V.K.; Williamson, S.S. Comprehensive review and comparison of DC fast charging converter topologies: Improving electric vehicle plug-to-wheels efficiency. In Proceedings of the 2015 IEEE 24th International Symposium on Industrial Electronics (ISIE 2015), Buzios, Brazil, 3–5 June 2015; pp. 263–268.
8. Musavi, F.; Edington, M.; Eberle, W.; Dunford, W.G. Evaluation and efficiency comparison of front end AC-DC plug-in hybrid charger topologies. *IEEE Trans. Smart Grid* **2012**, *3*, 413–421. [CrossRef]
9. Machiels, N.; Leemput, N.; Geth, F.; Van Roy, J.; Büscher, J.; Driesen, J. Design criteria for electric vehicle fast charge infrastructure based on flemish mobility behavior. *IEEE Trans. Smart Grid* **2014**, *5*, 320–327. [CrossRef]
10. Bai, S.; Lukic, S.M. Unified active filter and energy storage system for an MW electric vehicle charging station. *IEEE Trans. Power Electron.* **2013**, *28*, 5793–5803. [CrossRef]
11. Corchero, C.; Cruz-Zambrano, M.; Heredia, F.J. Optimal energy management for a residential microgrid including a vehicle-to-grid system. *IEEE Trans. Smart Grid* **2014**, *5*, 2163–2172.
12. Atia, R.; Yamada, N. Sizing and analysis of renewable energy and battery systems in residential microgrids. *IEEE Trans. Smart Grid* **2016**, *73*, 1204–1213. [CrossRef]
13. Lakshminarayana, S.; Xu, Y.; Poor, H.V.; Quek, T.Q. Cooperation of storage operation in a power network with renewable generation. *IEEE Trans. Smart Grid* **2016**, *7*, 2108–2122. [CrossRef]
14. Oliveira, T.R.; Silva, W.W.A.G.; Donoso-Garcia, P.F. Distributed secondary level control for energy storage management in dc microgrids. *IEEE Trans. Smart Grid* **2016**, 1–11. [CrossRef]

15. Falcones, S.; Ayyanar, R.; Mao, X. A DC–DC multiport-converter-based solid-state transformer integrating distributed generation and storage. *IEEE Trans. Power Electron.* **2013**, *28*, 2192–2203. [CrossRef]
16. Shin, C.J.; Lee, J.Y. An electrolytic capacitor-less bi-directional EV on-board charger using harmonic modulation technique. *IEEE Trans. Power Electron.* **2014**, *29*, 5195–5203. [CrossRef]
17. Rivera, S.; Wu, B.; Kouro, S.; Yaramasu, V.; Wang, J. Electric vehicle charging station using a neutral point clamped converter with bipolar DC bus. *IEEE Trans. Ind. Electron.* **2015**, *62*, 1999–2009. [CrossRef]
18. Liu, C.; Sun, P.; Lai, J.S.; Ji, Y.; Wang, M.; Chen, C.L.; Cai, G. Cascade dual-boost/buck active-front-end converter for intelligent universal transformer. *IEEE Trans. Ind. Electron.* **2012**, *59*, 4671–4680.
19. Tan, L.; Wu, B.; Rivera, S.; Yaramasu, V. Comprehensive DC power balance management in high-power three-level DC–DC converter for electric vehicle fast charging. *IEEE Trans. Power Electron.* **2016**, *31*, 89–100. [CrossRef]
20. *SAE Electric Vehicle and Plug-in Hybrid Electric Vehicle Conductive Charge Coupler*; J1772; SAE International: Warrendale, PA, USA, 2010.
21. Yilmaz, M.; Krein, P.T. Review of battery charger topologies, charging power levels, and infrastructure for plug-in electric and hybrid vehicles. *IEEE Trans. Power Electron.* **2013**, *28*, 2151–2169. [CrossRef]
22. Vasiladiotis, M.; Rufer, A. A modular multiport power electronic transformer with integrated split battery energy storage for versatile ultrafast EV charging stations. *IEEE Trans. Ind. Electron.* **2015**, *62*, 3213–3222. [CrossRef]
23. Dusmez, S.; Khaligh, A. A compact and integrated multifunctional power electronic interface for plug-in electric vehicles. *IEEE Trans. Power Electron.* **2013**, *28*, 5690–5701. [CrossRef]
24. Lu, X.; Iyer, K.L.V.; Mukherjee, K.; Kar, N.C. A dual purpose triangular neural network based module for monitoring and protection in Bi-directional off-board level-3 charging of EV/PHEV. *IEEE Trans. Smart Grid* **2012**, *3*, 1670–1678. [CrossRef]
25. Wang, Z.; Li, H. An integrated three-port bidirectional DC–DC converter for PV application on a DC distribution system. *IEEE Trans. Power Electron.* **2013**, *28*, 4612–4624. [CrossRef]
26. Kim, S.Y.; Song, H.S.; Nam, K. Idling port isolation control of three-port bidirectional converter for EVs. *IEEE Trans. Power Electron.* **2012**, *27*, 2495–2506. [CrossRef]
27. Kim, S.; Kang, F.S. Multifunctional onboard battery charger for plug-in electric vehicles. *IEEE Trans. Ind. Electron.* **2015**, *62*, 3460–3472.
28. Subotic, I.; Bodo, N.; Levi, E.; Jones, M.; Levi, V. Isolated chargers for EVs incorporating six-phase machines. *IEEE Trans. Ind. Electron.* **2016**, *63*, 653–664. [CrossRef]
29. Everts, J.; Krismer, F.; Van Den Keybus, J.; Driesen, J.; Kolar, J.W. Optimal ZVS modulation of single-phase single-stage bidirectional DAB AC–DC converters. *IEEE Trans. Power Electron.* **2014**, *29*, 3954–3970. [CrossRef]
30. Gu, B.; Lai, J.S.; Kees, N.; Zheng, C. Hybrid-switching full-bridge DC–DC converter with minimal voltage stress of bridge rectifier, reduced circulating losses, and filter requirement for electric vehicle battery chargers. *IEEE Trans. Power Electron.* **2013**, *28*, 1132–1144. [CrossRef]
31. Tan, X.; Ruan, X. Equivalence relations of resonant tanks: A new perspective for selection and design of resonant converters. *IEEE Trans. Ind. Electron.* **2016**, *63*, 2111–2123. [CrossRef]
32. Kheraluwala, M.N.; Gascoigne, R.W.; Divan, D.M.; Baumann, E.D. Performance characterization of a high-power dual active bridge DC-to-DC converter. *IEEE Trans. Ind. Appl.* **1992**, *28*, 1294–1301. [CrossRef]
33. Haihua, Z.; Khambadkone, A.M. Hybrid modulation for dual active bridge bi-directional converter with extended power range for ultra-capacitor application. In Proceedings of the IEEE Industry Applications Society Annual Meeting, Edmonton, AB, Canada, 5–9 October 2008; pp. 1–8.
34. Pinheiro, J.R.; Barbi, I. The three-level ZVS PWM converter-a new concept in high voltage DC-to-DC conversion. In Proceedings of the 1992 International Conference on Industrial Electronics, Control, Instrumentation, and Automation, San Diego, CA, USA, 13 November 1992; pp. 173–178.
35. Ruan, X.; Li, B.; Chen, Q. Three-level converters—A new approach for high voltage and high power DC-to-DC conversion. In Proceedings of the 2002 IEEE 33rd Annual IEEE Power Electronics Specialists Conference, Cairns, Queensland, Australia, 23–27 June 2002; Volume 2, pp. 663–668.
36. Steigerwald, R.L. A comparison of half-bridge resonant converter topologies. *IEEE Trans. Power Electron.* **1988**, *3*, 174–182. [CrossRef]

37. Kundu, U.; Yenduri, K.; Sensarma, P. Accurate ZVS Analysis for Magnetic Design and Efficiency Improvement of Full-Bridge LLC Resonant Converter. *IEEE Trans. Power Electron.* **2017**, *32*, 1703–1706. [CrossRef]
38. Hurley, W.G.; Wolfle, W.H. *Transformers and Inductors for Power Electronics: Theory, Design and Applications*; China Machine Press: Beijing, China, 2014; pp. 46–47.